Research in Astronomy and Astrophysics, 25:105011 (13pp), 2025 October
https://doi.org/10.1088/1674-4527/adf9a2
CSTR: 32081.14.RAA.adf9a2
© 2025. National Astronomical Observatories, CAS and IOP Publishing Ltd. All rights, including for text and data mining, AI training, and similar technologies, are reserved. Printed in China.

Particle Acceleration in the Outflow Region of Magnetic Reconnection on Solar Flare Loop-tops

Yan Li[1,2], Lei Ni[1,2], Jing Ye[1,2,3], and Zhixing Mei[1,2]
[1] Yunnan Observatories, Chinese Academy of Sciences, Kunming 650216, China; liyan821@ynao.ac.cn
[2] Yunnan Key Laboratory of Solar Physics and Space Science, Kunming 650216, China
[3] Yunnan Province China-Malaysia HF-VHF Advanced Radio Astronomy Technology International Joint Laboratory, Kunming 650216, China
Received 2025 May 24; revised 2025 July 15; accepted 2025 August 2; published 2025 September 5

Abstract

The origin of high-energy particles that generate non-thermal emission at the loop-tops of flare remains unclear. The loop-top regions of flares, which can be reached by outflows generated by magnetic reconnection, are prime candidate regions for the production of high-energy particles. In this work, we study particle acceleration within these regions by combining magnetohydrodynamics and test particle models. We focused on investigating the dynamic characteristics of particles in the two magnetic field configurations with and without a magnetic trap. In one case, the magnetic field contains a downward-concave structure formed by the collision of rapid reconnection outflows with closed magnetic loops, this structure is capable of confining particles for an extended period. Under the influence of the complex electromagnetic field distribution, the particles undergo multiple stochastic acceleration and deceleration processes. Ultimately, a small fraction of particles gain very high energies, while most particles exhibit only modest energy gains. We also observe two distinct particle distribution characteristics: the vast majority of particles are confined within the magnetic trap, with only a small number escaping from this region along open magnetic fields. Notably, the sharp bending of magnetic field lines at the exit of the magnetic trap triggers the aggregation of some particles. In the other case, the magnetic field in the reconnection outflow region does not include the magnetic concave structure, particles are difficult to capture and can quickly leave the outflow area along an open magnetic field. Regardless of the presence or absence of a concave structure, the energy spectra consistently exhibit the power-law distribution.

Key words: Sun: flares – Sun: particle emission – magnetohydrodynamics (MHD) – magnetic reconnection – acceleration of particles

1. Introduction

Solar flares are one of the most powerful energy-release processes in the solar system. It is widely believed that magnetic reconnection plays an important role in this process that converts the magnetic energy into thermal and kinetic energy of plasma, as well as accelerating charged particles (Benz 2017). During the solar flare, a large fraction of the released energy accelerates ions and electrons to energies up to tens of keV or even several GeV within seconds to minutes (Lin & Hudson 1976; Emslie et al. 2004; Aschwanden et al. 2017).

A portion of accelerated particles escapes into interplanetary space as the solar energetic particles that are detectable through the in situ measurements. At the same time, another fraction of energetic electrons and ions propagates sunward, colliding with the ambient solar atmosphere and generating hard X-ray emissions (including footpoint and loop-top sources) and γ-ray continuum, both of which are produced via bremsstrahlung processes. Notably, nuclear reaction line emissions are also observed, originating from physical processes such as nuclear de-excitation transitions, neutron capture reactions, and positron–electron annihilation (Kontar et al. 2011; Vilmer et al. 2011; Benz 2017). Masuda et al. (1994) reported the compelling evidence of the particle acceleration in flares for the first time according to the hard X-ray emission observed above the top of a soft X-ray loop. After that, the hard X-ray emission continues to be observed frequently above the loop-top sources (Petrosian et al. 2002; Krucker et al. 2010; Liu et al. 2013; Yu et al. 2020). On the other hand, the first evidence of flare γ-ray emission was provided by Chupp et al. (1973), and Hurford et al. (2003) presented the first γ-ray image of the solar flare (see also Vilmer et al. 2011 for a review on light curves of γ-ray emission as a result of the nuclear reactions).

Hard X-ray and γ-ray sources suggest energy release and particle acceleration in the corona with energetic particles that typically possess a power-law distribution of energy versus particle numbers. In most events, the light curves of γ-ray emission are very similar to those of the bremsstrahlung hard X-ray emission by energetic electrons, which indicates that the

acceleration and propagation of the flare-accelerated ions and electrons are closely related (Hurford et al. 2003). However, in some events, long-duration γ-ray flare/CME (also referred to as late-phase γ-ray emission) have also been detected, which are temporally and spectrally inconsistent with impulsive-phase nonthermal electron bremsstrahlung (Akimov et al. 1996; Share et al. 2018). Particle bremsstrahlung and γ-rays emissions only give the location where the interaction of particles with the atmosphere, not where the acceleration actually occurs. Hence, where the high-energy particles originate is still an open question. Although observations have provided a wealth of results on particle acceleration over a long history of study (e.g., see Raymond et al. 2012 for a review), there is still controversy how a large number of particles are rapidly accelerated to high energies within a short time.

Several acceleration mechanisms have been proposed to account for the particle acceleration during a solar flare. The most widely investigated ones are the acceleration by the electric field induced in the magnetic reconnecting current sheet, the stochastic acceleration by the plasma turbulence, and the shock acceleration in the outflow region (e.g., Aschwanden 2002; Benz 2008; Zharkova et al. 2011; Oka et al. 2018). However, no consensus has been reached currently on what kind of acceleration mechanism plays a major role at different stages and/or in different magnetic configurations in flare.

As magnetic reconnection involves robust electric currents, the super-Dreicer electric field remains a widely acknowledged mechanism for the acceleration of charged particles. The particle acceleration in the complex magnetic structure may be related to various reconnection current sheets, which may include structures of single or multiple X-type and O-type (magnetic islands) magnetic features with a guide field. In general, the combinations of magnetohydrodynamics (MHD) and test-particle methods have been used to study particle acceleration by magnetic reconnection (Onofri et al. 2006; Turkmani et al. 2006; Liu et al. 2009; Gordovskyy et al. 2010; Kowal et al. 2011; Li & Lin 2012; Yang et al. 2015; Zhou et al. 2016; Li et al. 2017, 2022; Xia et al. 2020). Meanwhile, the particle-in-cell (PIC) method, which is a self-consistent treatment of electromagnetic fields and particles, is also used to investigate particle acceleration by magnetic reconnection with conditions similar to those in the solar corona and flares (Drake et al. 2006; Siversky & Zharkova 2009; Hoshino 2012; Li et al. 2015; Xia & Zharkova 2020).

However, two approaches have their own suitable conditions due to limitations in computing power (Zharkova et al. 2011). The particle-in-cell method is crucial and powerful when simulating on the scale of the ion inertia. Alternatively, it is necessary to use the test particle method in the case that the length scale of the system is large compared to the ion inertial length, and the time interval of the system evolution is long compared to the ion cyclotron period. Given that the scale of flare structures is significantly larger than the typical dynamic scale (approximately tens of meters) in the corona, the test particle method is widely applied to particle acceleration on the macroscopic scales for the time being. However, some of the computational results between the two approaches are also extremely similar, such as particle energy spectra, trajectories, distributions, and so on. Recently, several methods and codes for accounting for the feedback of nonthermal fluids at the hydrodynamic scale have also been under development, such as the stochastic differential equations (Seo et al. 2024), the magnetohydrodynamic-particle-in-cell (Sun & Bai 2023), KGLOBAL (Drake et al. 2019), the relativistic hybrid particle-in-cell and Lattice boltzmann method (Zhu et al. 2020a, 2020b). These methods are currently in the testing phase and are capable of addressing multiscale problems and provide possible approaches for self-consistently studying magnetic reconnection and particle acceleration processes in the future.

During the two-ribbon flare, the region between the top of flare loops and the bottom of the current sheet is potentially another crucial location for particle acceleration (Chen et al. 2015; Fleishman et al. 2022). When the reconnection outflow exceeding the local fast magnetosonic speed collides with the closed magnetic field structure associated with the flare loop, a termination shock is generated. The termination shock is an important structure above the flare loops, observations and theory as well as numerical experiments suggest its existence (Tsuneta & Naito 1998; Warmuth et al. 2009; Li et al. 2013; Chen et al. 2015; Cai et al. 2019; Ruan et al. 2020; Ye et al. 2021). Kong et al. (2019) illustrated that electrons can be efficiently accelerated by the termination shock, and a magnetic trap on the loop top associated with the termination shock plays an important role in both accelerating and confining electrons. On the other hand, the strong turbulent electromagnetic fields generated by the collision between magnetic islands and the loop top also offer novel perspectives for understanding the origin of solar high-energy particles. Observations by Fleishman et al. (2022) demonstrated that a partial volume at the loop top is filled (or nearly filled) almost entirely with electrons having energies higher than 20 keV. They inferred that a strong super-Dreicer electric field played a crucial role in accelerating particles within that volume. However, systematic simulation studies in this specific context remain relatively sparse. Fully understanding how specific particles gain energy and how these high-energy particles manage to escape or be confined within the space they occupy still requires careful investigation.

Since the structural scale of magnetic reconnection in the flare actually far exceeds the inertial length of ion in the solar corona (e.g., see detailed discussions of Lin et al. 2015), we will integrate MHD numerical simulations with test particle methods to investigate the particle acceleration characteristics during the collision process between magnetic reconnection

outflow islands and flare loops in this study. Specifically, we first obtain the electromagnetic field configuration via MHD numerical experiments, then we track the motion of electrons and protons in this configuration. Because the timescale of the magnetic configuration is long compared to that of the particle acceleration, the configuration could be considered unchanged when we look into the dynamics of particles. Primarily, two cases are studied in which the configuration with and without the concave magnetic trap structure, and dynamic behavior of particles in two cases are compared. Our purpose is to comprehend the principal characteristics and inherent properties of particle acceleration in order to gain a deeper understanding of the acceleration of charged particles during solar flare events. In the next section, we introduce MHD and the particle acceleration model and formulae used in calculations. The results will be given and further analyzed in Section 3. Conclusions and short discussions of the work are presented in Section 4.

2. Numerical Methods and Computation Set-up

2.1. MHD Simulations

We start with 2.5-dimensional MHD numerical experiments to create a magnetic configuration. The setup used in the simulation is identical to that of Ni et al. (2015). The plasma is the fully ionized hydrogen gas that includes protons and electrons only, and the temperatures of these two species are the same. The numerical simulation is conducted using the NIRVANA code v3.6 (Ziegler 2011), with the implementation of the adaptive mesh refinement to enhance computational efficiency and accuracy. The initial magnetic field setup features a stationary, force-free Harris-type current sheet embedded with a guiding field. Meanwhile, the initial perturbations of both magnetic field and velocity are applied to speed up the reconnection process.

The characteristic values for the parameters are outlined below: the magnetic field strength is $B_0 = 10^{-3}$ T, the length scale is $L_0 = 10^8$ m, the mass density is $\rho_0 = 1.2 \times 10^{-12}$ kg m^{-3}, and the initial temperature is $T_0 = 10^6$ K. These characteristic values are selected to align with the typical properties of CME-flare current sheets as exemplified by Lin et al. (2015). Furthermore, other parameters, notably the Alfvén speed v_A and the characteristic timescale $t_0 = L_0/v_A$ relative to L_0 can be deduced accordingly. The dynamical viscosity coefficient is initially taken as $\nu = 10^{-5}/\rho_0$ m^{-2} s^{-1}, the initial magnetic diffusivity is $\eta_0 = 8 \times 10^7$ m^2 s^{-1}. Based on these values, we derive the Lundquist number S_0 to be approximately 1.0×10^6, and the plasma β is about 0.05. We specialize in conducting ultra-high resolution, adaptively refined 2.5D simulations.

In order to study the acceleration of particles, we need to obtain the configuration of the electromagnetic field. The electric field E is derived from the equation $E = \eta_e J - v \times B$ where η_e represents the electric resistivity of the plasma. Given the plasma velocity v, magnetic field B, and current density $J = \nabla \times B$ obtained from the MHD simulation, we can determine the electromagnetic field at any position and time using bilinear interpolation. According to the MHD simulation, we selected two different frames from results as the background electromagnetic field for studying particle acceleration. Figures 1(a) and (b) display the snapshots of the magnetic configurations at two different times of $t = 0.45$ and $t = 1.13$ after magnetic reconnection commences. These two snapshots respectively illustrate the existence and the absence of the concave magnetic trap structures inside the reconnection outflow region. Figures 1(c) and (d) display the corresponding enlarged local configuration and the distribution of the electric field in z-direction, respectively.

In the case of the concave magnetic trap absent (case A), the initial perturbation to the plasma flows in the x- and y-directions causes the reconnection process to occur gradually, giving rise to an increasingly thinner Sweet-Parker-like long current sheet. This process did not produce a concave magnetic trap structure in the outflow domain Figure 1(a), and the electric field in the reconnection region consists of two components: the conduction term $\eta_e J$ that dominates the region near the X-point, and the convection term $-v \times B$ that dominates the outflow region. In this case, the plasma outflow moves in the same direction, and the induced electric field is roughly in one direction as well Figure 1(c).

In the case of a concave magnetic trap occurring (case B), the aspect ratio of the current sheet increases, the tearing mode instability is invoked, leading to the fragmentation of the sheet into multiple pieces, and a series of magnetic islands associated with X-points form within the current sheet as depicted in Figure 1(b). These magnetic islands move upward or downward along the current sheet, with those moving downward colliding with the loop, thereby creating a concave magnetic trap area within which strong turbulence takes place. The direction of plasma velocity is constantly changing, causing strong electric fields to be generated in opposite directions in Figure 1(d). The electric field in this region allows charged particles to continuously experience processes of acceleration or deceleration. This results in an induced electric field of multiple directions in the area, and causes electrons and protons to be accelerated and decelerated in a stochastic manner.

In this work, we are dedicated to studying the detailed properties of particle acceleration in these two specific cases, aiming for a comprehensive understanding through analyses and simulations. Dynamic behavior of particles in the two electromagnetic field configurations will be investigated, and how the fine structures of the acceleration region influence the acceleration process and final energy gain of the particles will be studied in detail.

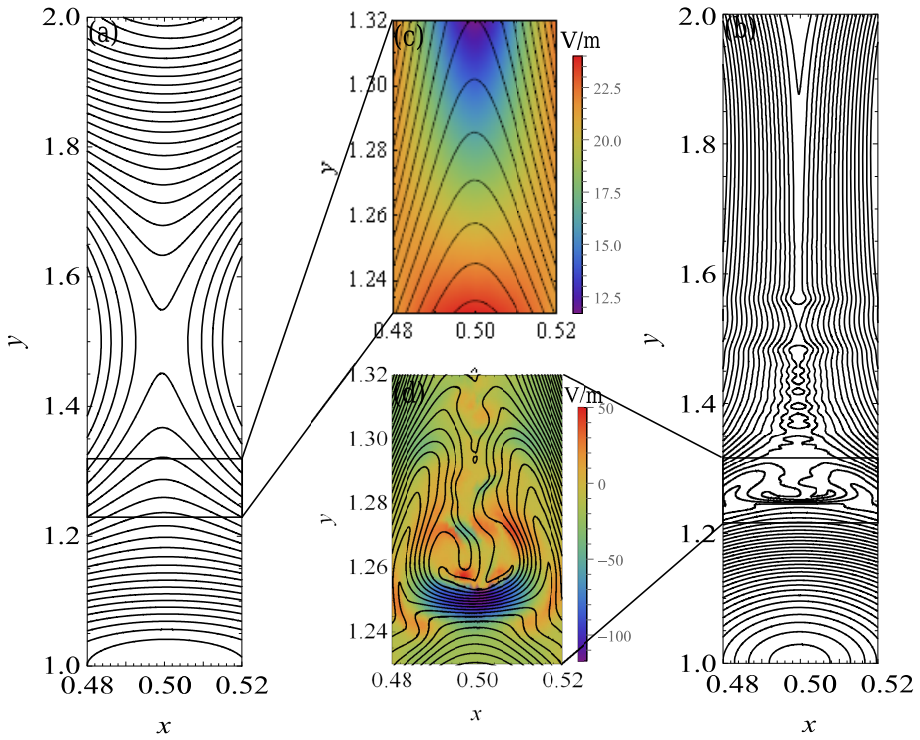


Figure 1. The snapshots of the configurations of magnetic field lines in xy-plane at two different times, which correspond to the times (a) $t = 0.45$, (b) $t = 1.13$, respectively. (c) and (d) display the enlarged image of the corresponding outflow area and the electric field distribution in the z-direction. The units in x- and y-direction are L_0.

2.2. Test Particle Approach

Usually, the particle acceleration timescale is less than 1 s. On the other hand, the typical time interval for the reconnecting magnetic configuration to evolve in the coronal environment is at least a few seconds. This indicates that the particle acceleration and transport processes occur at a much faster pace than the macroscopic evolution time of the eruption event. Therefore, we will use the quasi-static magnetic reconnection electromagnetic field in test-particle simulations during the solar eruption process.

In addition, the tenuous environment in the corona permits particles to move without undergoing collisions in the period of acceleration. Consequently, the motion of particles within the electromagnetic field is governed by the relativistic Lorentz equations:

$$\frac{dr}{dt} = \frac{p}{m\gamma} \tag{1}$$

$$\frac{dp}{dt} = q(E + u \times B), \tag{2}$$

where q is the electric charge of the particle, m is the rest mass of the particle. r, u and p are the position, the velocity, and the momentum of the particle, and $\gamma = 1/\sqrt{1 - u^2/c^2}$ is the Lorentz factor, c is the light speed. The characteristic values of various parameters are the same as those used for the numerical experiment.

In order to obtain trajectories of electrons and protons at different times via solving Equations (1) and (2), we need a set of the electromagnetic field configurations at different times. By conducting MHD simulations, we obtain the electromagnetic field at any specified location and time. For configurations not directly provided by the simulation results, an interpolation is used to deduce the configuration. We deliberately selected an identical area range to facilitate a meticulous comparison of the particle acceleration characteristics between case A and case B. As shown in Figure 1, the integration of Equations (1) and (2) is confined in the outflow domain of $0.48 < x < 0.52$ and $1.23 < y < 1.32$. Due to the symmetry of the system around the z-axis, all particles are initially positioned at $z = 0$. At each given time, about 7×10^5 test particles are initially distributed within this region uniformly. In order to compare with the results of the outflow zone, we will also use the same settings to investigate the energy spectrum distribution within the magnetic reconnection region (simulation domain: $0.48 < x < 0.52$ and $1.32 < y < 2.0$), where approximately 5×10^6 particles need to be calculated.

The initial velocity of particles follows the Maxwellian distribution corresponding to the typical solar corona

temperature $T_0 = 10^6$ K. Then, we use the fourth-order Runge–Kutta–Fehlberg scheme with the adaptive time step to solve Lorentz equations. Each integration of the equations for a test particle continues until the particle leaves the domain via any one of the four boundaries. If a test particle still stays in the domain for $t > 0.01t_0$ ($\sim$1.27 s), we considered it trapped and the corresponding simulation terminated as well. The time-scale of this is much shorter than the overall evolution of solar flares, which justifies the use of static MHD. The kinetic energy of particles obtained from the acceleration is calculated using the formula $\xi_k = (\gamma - 1)mc^2$. In the present work, we do not consider the loss of particle kinetic energy due to radiation and collisions with other particles or plasma. Instead, the gain and loss of energy for individual particles occur solely through their interactions with the electromagnetic field within the reconnection outflow region.

3. Characteristics of Particle Acceleration

In this section, we will investigate the kinematic behavior of particles that are accelerated by the electromagnetic field (as depicted in Figure 1) within the reconnection outflow region. We are looking into several aspects: trajectories of particles in the reconnection outflow region, the final spatial distribution of particles versus energy, the specific relationship between the final energy of particles and their residence time within the computational domain, as well as the characteristics of the particle energy spectrum. Specifically, we focus on the impact of the concave magnetic trap structure on these aspects, aiming to reveal how the presence or absence of the traps alters the dynamic behavior of particles. This will provide crucial information about the energy distribution and dynamic behavior of particles under specific conditions.

3.1. Trajectories of Protons

The mass difference between electrons and protons may lead to disparities in acceleration time, scale, and ultimately the energy acquired. Due to the opposite charge polarities, their motion and acceleration directions along the electric field, as well as the drift motions of the particles (such as curvature or gradient drifts), all exhibit characteristics of being in opposite directions. Simultaneously, in the presence of a strong guide magnetic field, accelerated electrons and protons also demonstrate significant spatial separation. These dynamics, driven by differences in charge polarity, result in electron and proton trajectories displaying mirror-like symmetry in space. Several authors have provided detailed descriptions of particle motion in electromagnetic fields, particularly in X-point configurations (e.g., Zharkova & Gordovskyy 2004; Yan et al. 2013). To avoid redundancy in presenting these established results, we merely present proton trajectories in this paper for illustrative purposes.

Case A: Figures 2(a) and (b) depict the typical trajectories of protons injected from different positions in the xy-plane, and the corresponding energy as a function of time is shown in Figures 2(c) and (d), and the three-dimensional trajectory diagrams of the particles are shown in Figures 2(e) and (f). We can see that some protons exit the acceleration area quickly, while others undergo multiple back-and-forth motions before leaving. The protons generally follow the contours of large-scale magnetic field and oscillate in the x-direction, accompanied simultaneously by the drift phenomena in the other direction.

In the outflow region below the X-point, rapidly flowing plasma generates an electric field by $-v \times B$. This electric field subsequently induces the $E \times B$ drift. As a result, protons are able to cross or deviate from magnetic field lines, leading to drift in the y-direction. Meanwhile, Figure 2(b) also indicates that the particles have undergone magnetic mirror effects due to the influence of the converging magnetic field. Thus, protons exhibit oscillatory motion along the magnetic field lines in the outflow region. In general, the oscillation along the magnetic field lines, while the slight drift toward the X-point domain constitute the principal motion characteristics of particles in the absence of concave magnetic structures. Subsequently, the particles quickly leave the simulation area along the open magnetic field lines.

Although the electric field in the current sheet determines the gain or loss of energy, the magnetic field not only guides the trajectory of particles, but also indirectly affects the acquisition of energy. According to Figure 1(c), it can be seen that the electric field maintains the same direction during this stage. However, the magnetic field has a significant impact on the energy gain of particles, causing them to gain or lose energy alternately Figures 2(c) and (d). This ensures that any energy loss does not completely exhaust the total energy previously obtained, ultimately leading them to exit from the acceleration area with a net increase in energy.

In Case A, the guiding field is oriented along the z-direction with a relatively weak intensity ($10^{-5}B_0$). The inset of Figure 2(c) depicts the temporal evolution of particle energy in the x, y, and z directions. It can be seen that the energy gain in the z-direction is predominant, while the xy-plane exhibits a secondary contribution.

Case B: When a rapidly moving magnetic island collides with a loop structure, it generates a highly turbulent magnetic depression, which in turn produces an extremely complex and varied electromagnetic field distribution as shown in Figure 1(d). In this complex electromagnetic environment, positive and negative electric fields act as accelerators or brakes, respectively speeding up or slowing down particles. Meanwhile, the magnetic field governs the motion pattern of particles. The combination of the impacts of the magnetic field and electric field on the motion of particles results in extremely

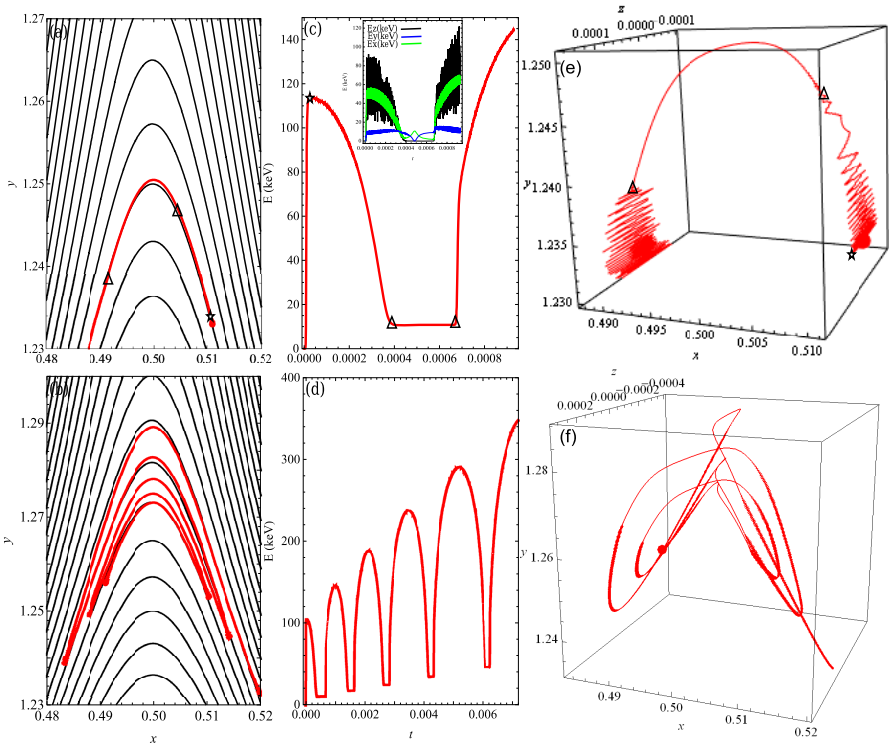


Figure 2. The left column shows the trajectories of accelerated protons in the magnetic fields. The corresponding particle energy vs. time are arranged in the middle column. The right column displays the 3D trajectories of particles. The inset in panel (c) shows the energy variations of the particles in the x, y, and z directions. The initial location of each particle is denoted by the red dot.

complex trajectories and a variety of rich dynamic characteristics for particles.

Figure 3 shows the motion features of particles within the magnetic concave structure. In this case, the trajectory that strikes any one of the four boundaries of the calculation domain signifies particles that have been accelerated but remains uncaptured, and finally depart from the acceleration domain Figures 3((a), (e)). On the other hand, the trajectories of particles that remain within the calculation domain represent those particles that have been captured within the acceleration timescale in Figures 3((b), (f)). Compared with case A, it can be clearly observed that the magnetic concave structure exhibits a special effect, namely, it significantly enhances the ability of the relevant magnetic structure to retain particles within the acceleration region. This structure acts as a "magnetic trap" for particles, preventing them from leaving the acceleration region easily and allowing them to obtain a longer retention time.

The corresponding variations of particle energies versus time are shown in Figures 3(c) and (d), respectively. Turbulent behavior within the electromagnetic field of the acceleration region results in particles stochastically gaining or losing energy. Importantly, throughout this process, the energy previously acquired by the particles is not completely depleted at any stage. Consequently, these particles will inevitably encounter two possible situations: either exit the acceleration zone with a net energy gain or remain trapped within the acceleration zone. In these two cases, turbulence in the outflow region governs the dynamic properties of particles as well as the efficiency of the associated energy gain. Regardless, particles can always obtain more or less net energy from this electric field. It should be noted that the particles selected for this study are representative of typically accelerated particles. In reality, the majority of particles either captured within or exiting the domain have energies not very different from their initial energies at the end of the calculation. Only a few particles are ultimately accelerated to energies much higher than their initial thermal velocity, and specific discussions will be presented in the next subsection.

The typical spatial inhomogeneity scale of the polarity inversion line in flare loops/arches along the z-direction is on the order of a few Mm (Zimovets et al. 2013; Li & Zhang 2015; Ledentsov 2023). Figures 2 and 3 demonstrate that during the acceleration process, particles exhibit oscillatory motion characteristics in the positive and negative z-directions. High-energy particles (>100 keV) show travel distances on the order of 10^4–10^5 m. Therefore, the spatial inhomogeneity along the z-direction can be neglected.

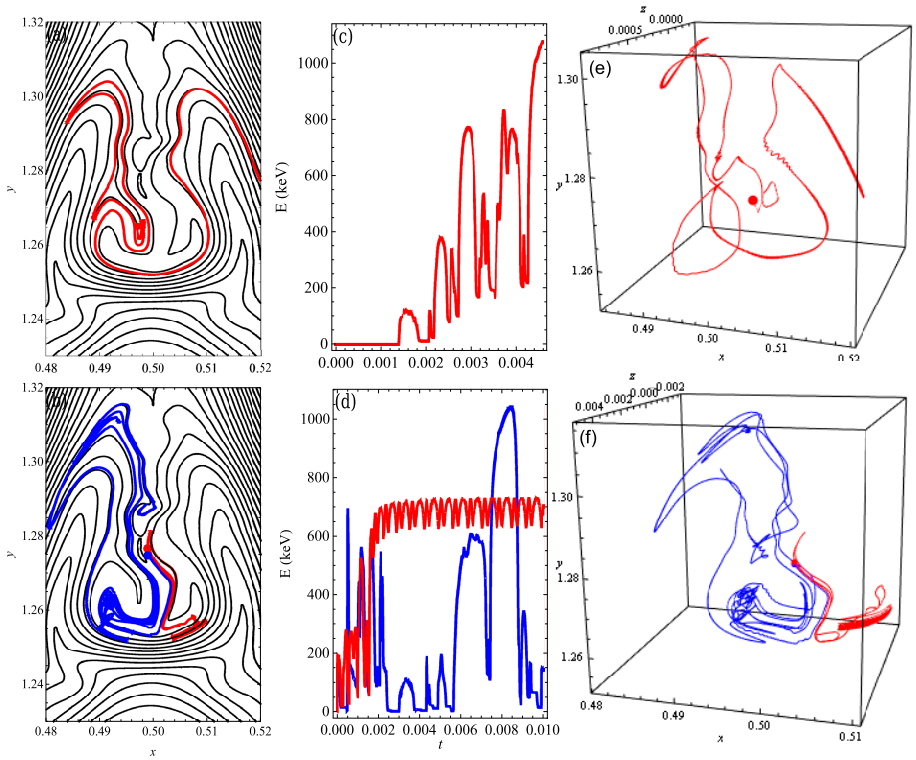


Figure 3. Same as Figure 2 but for case B. The trajectories of particles in the magnetic trap structure are shown.

3.2. Particle Energy Spectra

From the results of MHD numerical simulations, we meticulously selected the background electromagnetic fields at two specific times to examine how the test particles behave within those two electromagnetic fields (Figure 1). We investigated the energy spectrum distribution of electrons and protons according to the calculation settings given in Section 2. In the calculation, when particles move to the boundary of the simulation, they are considered to have escaped from the system, and their final energies are recorded. When the calculation ends, the energy state of particles that still remain in the acceleration region can also be obtained. Both of these (i.e., the total initial number of particles) are used together to calculate the particle energy spectrum. When the calculation stopped, in Case A, approximately 93.1% of electrons and 74.3% of protons left the simulation region; in Case B, however, only 8% of electrons and 5.3% of protons left. The energy spectra of particles manifest a double logarithmic fashion as shown in Figure 4 for both electrons and protons. The upper panels are for case A, and the lower panels are for case B. The red curve is for the results of acceleration occurring in the outflow region ($1.23 < y < 1.32$ and $0.48 < x < 0.52$), whereas the black curve reflects acceleration within the current sheet ($1.32 < y < 2.0$ and $0.48 < x < 0.52$) to compare the differences in acceleration between the two regions.

From the energy spectrum diagram, it can be seen that the particle distribution exhibits significant characteristics. Specifically, most of the particles are concentrated in the relatively low-energy range, which indicates that these particles have not undergone substantial acceleration processes. Subsequently, the number of accelerated particles decreases rapidly, though their energy gain increases by several orders of magnitude. That is to say, the higher the energy, the fewer the number of accelerated particles.

We employ a single power-law fitting function $E^{-\delta}$, using energies >200 keV for protons and >20 keV for electrons as the starting points for the fits, aiming to encompass the subsequent higher energy ranges as comprehensively as possible. Due to the limited particle statistics in the high-energy tail region, the fitting results may carry inherent uncertainties. Therefore, our analysis primarily focuses on the intermediate energy range, where non-thermal particle statistics are sufficient, and the results are relatively reliable. In the stage of case A, the spectral indices δ deduced from fitting the spectrum to the power-law distribution are $\delta \sim 1.3$ and 1.77 for electrons and protons, respectively. In the stage of case B, the energy spectra have δ of 1.63 and 1.45 for electrons and protons, respectively. We further notice that the highest energy of electrons and protons could reach up to 800 keV (Figure 4(c)) and 7 MeV (Figure 4(d)), respectively, in case B; while the maximum energy attained is only near 700 keV

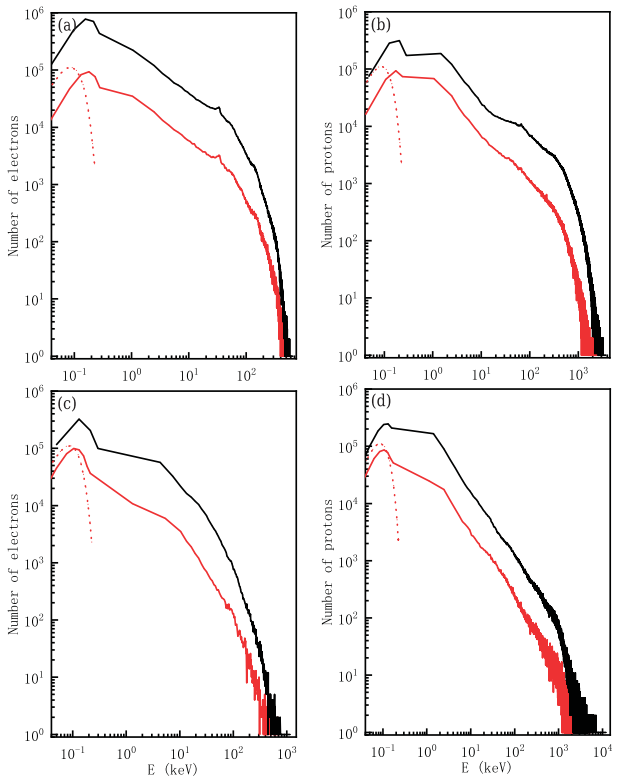


Figure 4. Distribution function for all the particles injected in the domain at the end of the simulations. The black and red curves in all four panels correspond to the acceleration situation in the current sheet and in the outflow area, respectively. Meanwhile, panels (a) and (b) respectively display the distribution of electrons and protons during the process of X-point reconnection. Conversely, within the area characterized by a magnetic trap structure, panel (c) portrays the electron distribution, whereas panel (d) depicts the distribution of protons. In each panel, the dotted line represents the initial distribution of particles in the outflow region.

and 2.5 MeV, respectively, as shown in Figures 4(a) and (b) in case A.

On the other hand, we can clearly observe significant similarities in their energy distribution characteristics by comparing and analyzing the energy spectra of the outflow region and the current sheet. Notably, the maximum energy attainable by particles within the current sheet is slightly higher than that in the outflow region. The comparative analysis of electric field intensity indicates significant differences between the current sheet region and the outflow region. Measurement data show that the peak electric field strength in the current sheet can reach up to 187 V m^{-1}, while the maximum electric field strength in the outflow region is only 120 V m^{-1}. This result confirms that the current sheet region possesses a stronger electric field distribution characteristic. At the same time, more efficient particle acceleration mechanisms, such as multiple X-points (magnetic reconnection sites) and magnetic islands, are present in the current sheet (Drake et al. 2006; Oka et al. 2010; Li et al. 2015; Li et al. 2022). Another possibility is that the current sheet area ($1.32 < y < 2.0$) is approximately 7.5 times larger than the outflow domain under consideration ($1.23 < y < 1.32$). This implies that particles can remain there longer and thus gain higher energies. These processes work together to enable particles to gain higher energies within the current sheet.

As illustrated in Figures 2 and 3, the energy required to construct the spectrum is derived from two distinct cases: the final energy of particles remaining in the acceleration region at the end of the calculation, or the energy of particles when they exit the acceleration region. It is imperative for us to develop a profound understanding of the specific contributions made by these two categories of particles to the composition of the energy spectrum. Figure 5 depicts the relationship between the final energy of protons and electrons and the time interval during which they remain within the structures of case A and case B.

We clearly observe two potential evolutionary outcomes for particles during the acceleration phase: First, when $t < 0.01$, some particles, regardless of their acquired energy, successfully escape the acceleration region. These particles may be ejected along specific trajectories, breaking free from the confinement of the acceleration region. On the other hand, the remaining particles had failed to escape the acceleration region and remained confined within it by the end of the simulation ($t = 0.01$). It is during this brief time interval that they may be subjected to magnetic confinement, leading to significant alterations in their trajectories. After undergoing a series of complex physical processes, these particles ultimately remain trapped within the region, and their acquired energies exhibit significant differences.

The X-point magnetic configuration, more conducive to particle escape, clearly shows a significantly higher number of escaping electrons and protons in case A compared to case B, as evidenced by the comparison between Figures 4(a) and (b), and Figures 4(c) and (d). Furthermore, it is also found that the particles trapped within the simulation region exhibit an average energy level markedly higher than that of the escaped particles. This indicates that, after undergoing a series of intricate physical processes, some of these captured particles have acquired additional energy. For example, in case A, the trapped electrons and protons reach energies of up to 700 keV and 2.5 MeV in Figures 5(a) and (b), respectively. In contrast, those escaping along the open field lines are accelerated only to approximately 600 keV and 1.6 MeV, respectively. We quantified the energy conversion efficiency between escaping and confined particles: For electrons, the mean energy ratio of final-to-initial states was 11:1 for escaped electrons, compared to 27:1 for confined electrons. For protons, this ratio increased to 79:1 for escaped protons, while reaching 101:1 for confined protons. Additionally, case B also exhibited comparable results. Thus, we can realize that the high-energy component of the power-law spectrum originates from particles confined

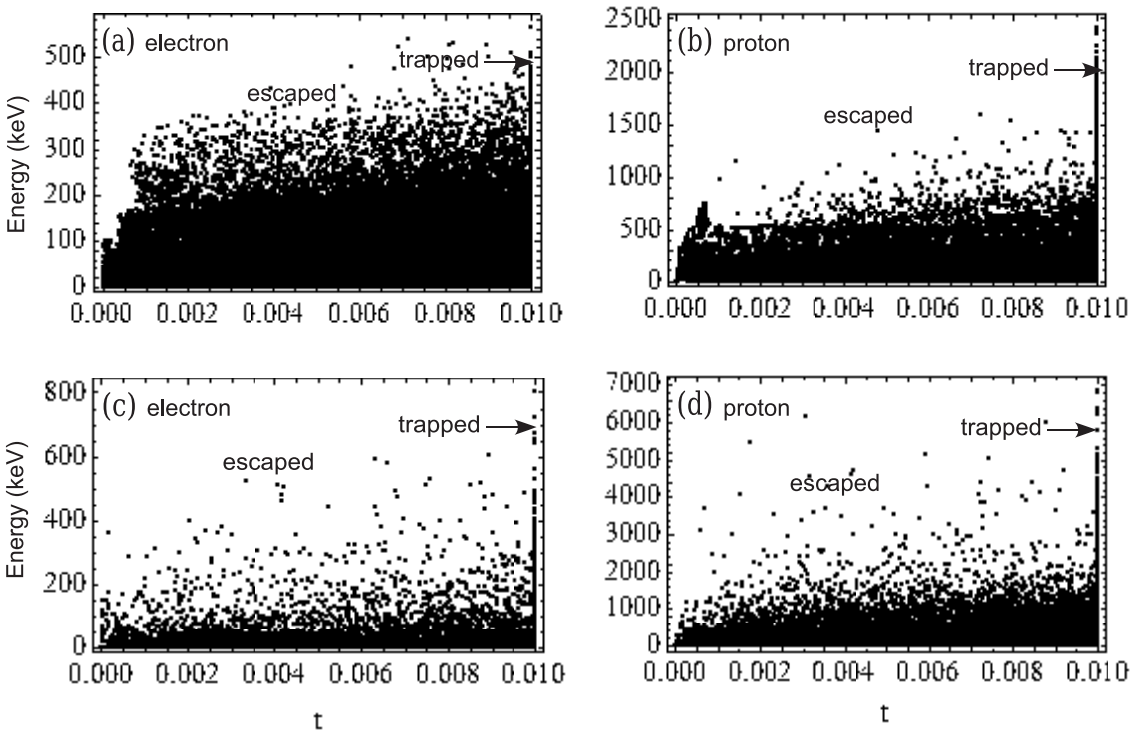


Figure 5. The energy of electrons and protons as they leave the computational domain as a function of time, respectively. (a) and (b) correspond to case A, and (c) and (d) for case B. Each dot represents a single particle.

within the outflow region, whereas the escaped and partially confined particles are responsible for the lower-energy component of the spectrum.

If the particle injection direction is the same as the electric field, these particles undergo direct acceleration, with their energy gain far exceeding the initial low-energy state. Conversely, if the injection direction is opposite to the electric field, the particles first decelerate and lose part of their initial thermal energy before being reaccelerated by the electric field. During this period, all these processes lead to differences in the net energy gained by the particles, and some particles will inevitably leave the acceleration region quickly. After that, if some particles continue to reside within the acceleration region, they will encounter alternating electric fields or complex magnetic structures, causing them to undergo stochastic acceleration and deceleration, thereby delaying the time required for them to escape from the region. The result of this process is that only a few particles achieve a significantly noticeable net energy increase, while the energies of the remaining particles exhibit a slow, oscillatory trend of gradual increase.

3.3. Spatial Distributions of Accelerated Particles

Due to the distinct electromagnetic field distributions in the two acceleration regions of case A and case B, the spatial distribution of energetic particles also exhibits significant variations during the simulation process. A detailed investigation of the distribution characteristics of particles in space is important for a comprehensive and profound understanding of the particle acceleration mechanism. Figures 6 and 7 display the spatial distributions of energetic electrons and protons projected onto the x–y plane in case A and case B, respectively.

In case A, the open magnetic configuration allows the accelerated particles to escape easily. Figure 6 clearly illustrates that most particles could escape from the acceleration region roughly along the magnetic field lines, while only a small number of particles remain trapped within the acceleration region. Ultimately, particles remaining in the acceleration region form a distribution pattern around these open field lines, and particles with higher energies exhibit a stronger tendency to distribute along the magnetic separatrix (as shown in Figure 2). However, their acceleration times differ from each other due to the distinct difference between their masses. Electrons, being lighter than protons, are more easily accelerated, allowing them to reach relativistic speeds in a short time interval, and enabling them to swiftly exit the acceleration zone. In contrast, protons need to take longer time to be accelerated, resulting in a large number of protons remaining in the acceleration area compared to electrons.

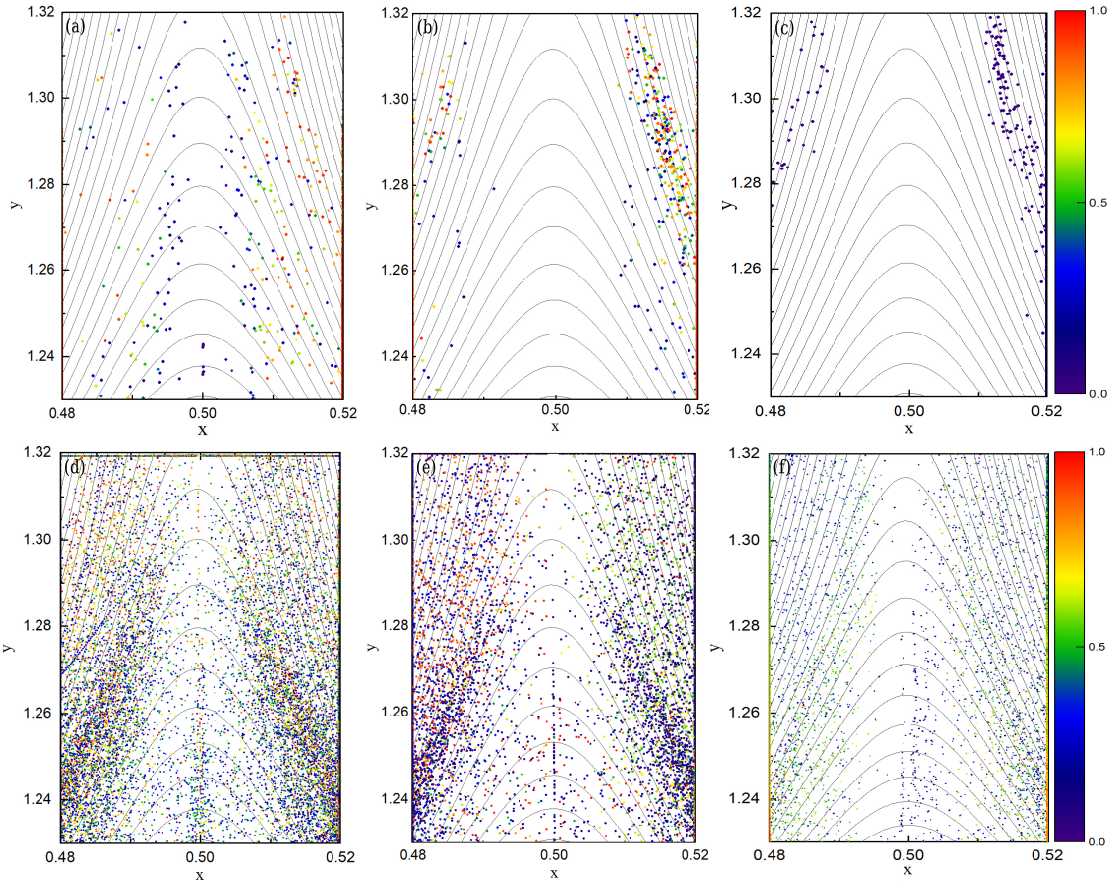


Figure 6. The spatial distribution of accelerated electrons and protons at different energies in case A. Panels (a), (b), and (c) show the distribution of electrons with three energy ranges 20 keV $< E <$ 60 keV, 60 keV $< E <$ 100 keV, 100 keV $< E <$ 400 keV, respectively. Panels (d), (e), and (f) show the distribution of protons with energy ranges 50 keV $< E <$ 200 keV, 200 keV $< E <$ 1 MeV, 1 MeV $< E <$ 2.5 MeV, respectively. The color scale is normalized to the maximum particle energy of each individual image.

Another phenomenon is the asymmetry of particle distribution, which has been demonstrated by some authors through trajectory calculations to show the asymmetry of particle ejection in the presence of a guiding field (e.g., Zharkova & Gordovskyy 2004; Yan et al. 2013; Xia et al. 2020). In our results, the upper three panels in Figure 6 display the distribution of electrons in the calculation region. Low-energy electrons (left panel) exhibit an approximately symmetric distribution about $x = 0.5$ with primary concentration confined to the region between 0.495 and 0.505. In Case A, the guide field is approximately $10^{-5}B_0$ and oriented along the positive z-direction. Zharkova & Gordovskyy (2004) analyzed the asymmetry of particle acceleration in the reconnection current sheet. Their results demonstrate that the particle outflow direction is proportional to $q^3B_xB_zE$, and the weaker the guiding field, the lower the asymmetry rate. In case A, q and B_x are negative, while weak B_z and E are positive, which will cause partial separation of electrons and mainly flow toward the right boundary. As the energy increases, the asymmetry becomes more and more apparent. The most energetic electrons mainly choose to leave the acceleration domain from the upper right corner (right panel). On the other hand, protons do not exhibit this behavior clearly due to their large mass and the weak background guiding field.

For case B, Figure 7 shows the particle distribution in the presence of a magnetic trap. Since particles cross magnetic field lines with difficulty, they are strongly confined in this case and involved in complex interactions during their attempt to escape from a concave structured magnetic field, which slows down the escape process. In case B, the acceleration region includes the concave structure, and particles are confined around this structure and are involved in complex interactions with fine structures of magnetic field around. Consequently, particles struggle to leave this region within the limited time. It is evident that, compared with case A as shown in Figure 6, electrons and protons remain confined within the concave region and many low-energy particles distributed widely in the calculation domain. As their energy increases,

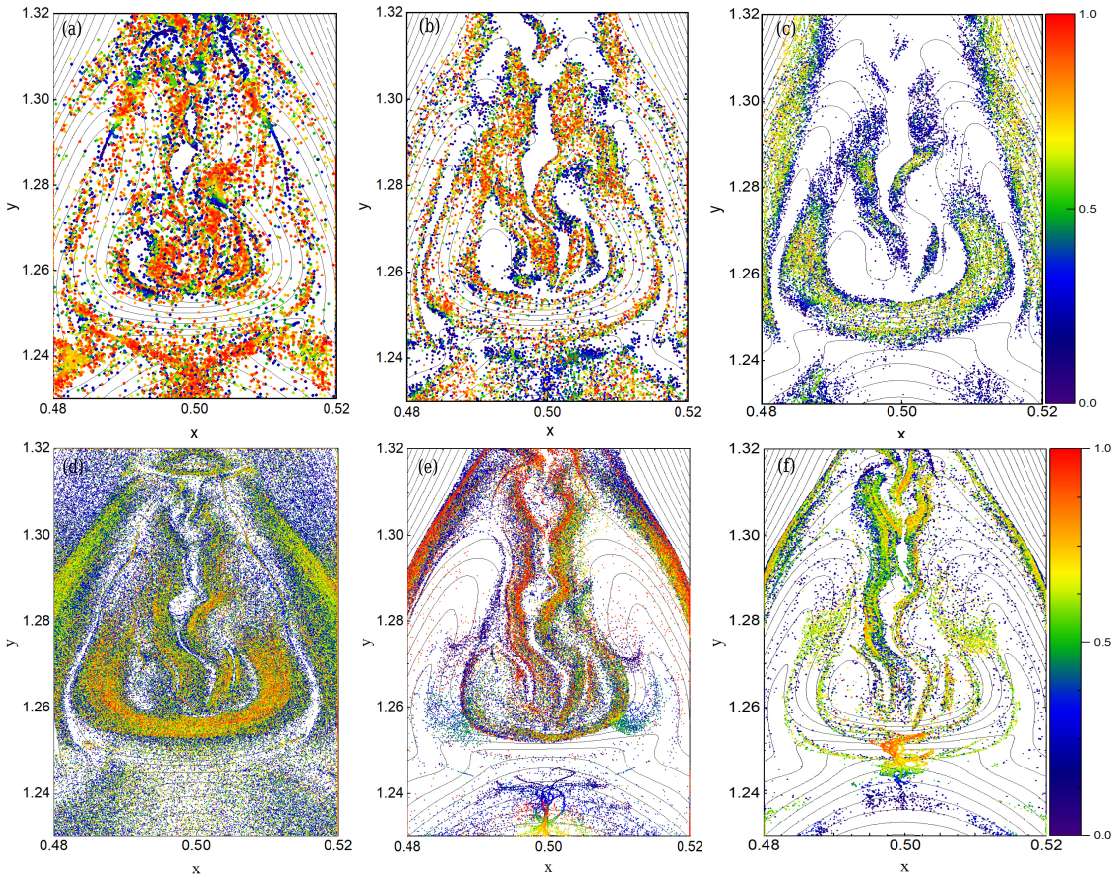


Figure 7. Same as Figure 6 but for case B. The electron energy ranges of panels (a), (b), and (c) are 20 keV $< E <$ 60 keV, 60 keV $< E <$ 100 keV, 100 keV $< E <$ 400 keV, respectively. Panels (d), (e), and (f) show the distribution of protons with energy ranges 50 keV $< E <$ 200 keV, 200 keV $< E <$ 1 MeV, 1 MeV $< E <$ 7 MeV, respectively.

however, the number of particles decreases and the distribution becomes more concentrated in a smaller space. In other words, particles with higher energy have smaller numbers and more concentrated distribution. Despite the extreme complexity of the electromagnetic field, particles typically still follow a distribution along the magnetic field lines. Unlike in case A, these particles do not exhibit any significant bias in direction as they leave the acceleration region, indicating an absence of noticeable jet asymmetry.

Additionally, another phenomenon can be observed: When particles escape from the magnetic trap, a subset of particles exhibits a pronounced tendency to accumulate near the exit of the magnetic trap, which originates from the severe bending of magnetic field lines in this region. Since particles primarily move along the direction of magnetic field lines, when the magnetic field direction changes rapidly, particles are forced to continuously alter their direction of motion, thereby hindering their migration process and forming complex motion characteristics. When particles approach this curved magnetic field region during their escape from the magnetic trap, the combined effect of rapidly changing magnetic field gradients and curvature causes some particles to exhibit a phenomenon of accumulation and retention near the trap's exit, making it difficult for them to escape quickly. This phenomenon highlights the significant impact of severely bent magnetic field lines on the motion and distribution of particles, allowing for a more detailed understanding of the behavior of particles in magnetic traps.

4. Summary and Discussion

In this study, we utilized 2.5D MHD numerical simulations of magnetic reconnection with realistic solar flare physical parameters to successfully obtain self-consistent and reasonable electromagnetic field configurations in the outflow region. To further investigate the behavior of charged particles within these fields, we meticulously chose two key "snapshots" of magnetic and electric fields from the simulations: one featuring a magnetic trap structure, and the other without. By applying the test particle method, we investigated in detail the acceleration and motion characteristics of charged electron and proton under these two different electromagnetic field

configurations. Our findings offer valuable insights into the dynamics of particles during solar flares.

In the absence of a magnetic trap structure, particles quickly escape the acceleration region after a brief period of acceleration. By the end of the calculation, most particles have left, making it difficult for particles to aggregate within the region, thereby significantly reducing the formation of particle clustering effects. The presence of a magnetic trap temporarily captures and confines particles within the simulation domain. During their motion, particles are subjected to alternating electric fields in opposite directions, leading to continuous energy gain or loss. The interaction between electromagnetic fields and particles causes most particles to remain in the computational domain for longer after undergoing stochastic processes, becoming confined within the magnetic trap, yet only a small fraction of these particles experience a significant net increase in energy. This structure indicates that, during the simulation process, the magnetic trap structure exhibits high efficiency in confining particles, yet it is unable to sustain an infinite increase in particle energy.

Both electromagnetic field structures can accelerate particles, enabling a small fraction of electrons and protons to rapidly reach relativistic energies within an extremely short time. The energy distribution of the accelerated protons and electrons exhibits a single power-law form. The high-energy component of the power-law spectrum originates from particles confined within the outflow region, whereas the escaped and partially trapped particles are responsible for the lower-energy component of the spectrum. In case A, most particles will escape quickly, and lighter electrons also exhibit asymmetry when ejected. In case B, most electrons and protons are still confined within the simulation area when the calculation ends. Meanwhile, as energy increases, the number of particles decreases and their distribution becomes more concentrated. A noteworthy phenomenon is that some leaving particles, upon reaching the exit of the magnetic trap, are affected by a sharp bending of the magnetic field lines, leading to their aggregation.

The magnetic reconnection outflow region is one of the important regions where high-energy particles are generated. However, in the absence of an effective confinement mechanism, these particles will rapidly propagate to the footpoints, making it difficult to form a radiation source at the top of the loop (e.g., as described in case A). When the fast reconnection outflow collides with the flare loop, a collapsed magnetic trap may be generated (case B). The subsequent emergence of magnetic traps may offer a plausible explanation for the delayed appearance of flare loop-top sources as compared to footpoint sources (Melnikov 2006). Kong et al. (2019) investigated particle acceleration by termination shock in the vicinity of magnetic traps, whereas our research aims to reveal the crucial role of turbulent electric fields in the outflow region in driving particle acceleration, and to explore how the presence or absence of magnetic traps influences the formation of radiation sources at the loop top.

Nonthermal hard X-ray and microwave emission (including sources at the footpoints and loop-top) can be recognized as the remarkable evidence for the production of energetic particles. Krucker et al. (2010) provides a detailed hard X-ray and microwave observations. Their results suggest that the above-the-loop-top source is the acceleration region itself. Meanwhile, they speculate that above-the-loop top sources are only visible once all electrons are accelerated. The electric field inferred by Fleishman et al. (2022) based on magnetic field decay is approximately 20 V cm^{-1}; this strong super-Dreicer electric field works over literally all ambient particles, which boosts their energies to 20 keV and higher. These findings indicate that high-energy particles generated within the outflow region require extremely high acceleration efficiency.

Observations by Fleishman et al. (2022) reveal that the loop-top region not only confines electrons within it but also accelerates most electrons to energies exceeding 20 keV via strong induced electric fields—a result implying high acceleration efficiency. However, in our simulations (case B), only approximately $\sim$16% of electrons (>20 keV) and about $\sim$3.5% of protons (>200 keV) were accelerated from the initial thermal plasma distribution. Therefore, the efficiency of particle acceleration is still too low to match the observed results of almost all particles being accelerated (Fleishman et al. 2022). Naturally, if the acceleration efficiency is low or the escape rate of accelerated particles is high, the excited hard X-rays will be relatively weak. If they are below the present-day detection limit, they will be difficult to observe. To improve understanding of acceleration efficiency, more realistic simulations and various acceleration mechanisms may constitute valuable issues for future work.

Acknowledgments

This research is supported by the Strategic Priority Research Program of the Chinese Academy of Sciences with grant No. XDB0560000; the National Key R&D Program of China No. 2022YFF0503800; the NSFC grants 12373060, 12073073, 42274216, 11933009, and 12273107; the Yunling Scholar Project of Yunnan Province and the Yunnan Province Scientist Workshop of Solar Physics; and Yunnan Key Laboratory of Solar Physics and Space Science under No. 202205AG070009. We gratefully acknowledge our discussions with Jun Lin. The numerical calculations and data analysis have been done in the Computational Solar Physics Laboratory of Yunnan Observatories.

References

Akimov, V. V., Ambrož, P., Belov, A. V., et al. 1996, SoPh, 166, 107
Aschwanden, M. J. 2002, SSRv, 101, 1

Aschwanden, M. J., Caspi, A., Cohen, C. M. S., et al. 2017, ApJ, 836, 17
Benz, A. O. 2008, LRSP, 5, 1
Benz, A. O. 2017, LRSP, 14, 2
Cai, Q., Shen, C., Raymond, J. C., et al. 2019, MNRAS, 489, 3183
Chen, B., Bastian, T. S., Shen, C., et al. 2015, Sci, 350, 1238
Chupp, E. L., Forrest, D. J., Higbie, P. R., et al. 1973, Natur, 241, 333
Drake, J. F., Arnold, H., Swisdak, M., & Dahlin, J. T. 2019, PhPl, 26, 012901
Drake, J. F., Swisdak, M., Che, H., & Shay, M. A. 2006, Natur, 443, 553
Emslie, A. G., Kucharek, H., Dennis, B. R., et al. 2004, JGRA, 109, A10104
Fleishman, G. D., Nita, G. M., Chen, B., Yu, S., & Gary, D. E. 2022, Natur, 606, 674
Gordovskyy, M., Browning, P. K., & Vekstein, G. E. 2010, ApJ, 720, 1603
Hoshino, M. 2012, PhRvL, 108, 135003
Hurford, G. J., Schwartz, R. A., Krucker, S., et al. 2003, ApJL, 595, L77
Kong, X., Guo, F., Shen, C., et al. 2019, ApJL, 887, L37
Kontar, E. P., Brown, J. C., Emslie, A. G., et al. 2011, SSRv, 159, 301
Kowal, G., de Gouveia Dal Pino, E. M., & Lazarian, A. 2011, ApJ, 735, 102
Krucker, S., Hudson, H. S., Glesener, L., et al. 2010, ApJ, 714, 1108
Ledentsov, L. S. 2023, AstL, 49, 744
Li, G., Kong, X., Zank, G., & Chen, Y. 2013, ApJ, 769, 22
Li, T., & Zhang, J. 2015, ApJL, 804, L8
Li, X., Guo, F., Li, H., & Li, G. 2015, ApJL, 811, L24
Li, Y., & Lin, J. 2012, SoPh, 279, 91
Li, Y., Ni, L., Ye, J., Mei, Z., & Lin, J. 2022, ApJ, 938, 24
Li, Y., Wu, N., & Lin, J. 2017, A&A, 605, A120
Lin, J., Murphy, N. A., Shen, C., et al. 2015, SSRv, 194, 237
Lin, R. P., & Hudson, H. S. 1976, SoPh, 50, 153
Liu, W., Chen, Q., & Petrosian, V. 2013, ApJ, 767, 168
Liu, W. J., Chen, P. F., Ding, M. D., & Fang, C. 2009, ApJ, 690, 1633
Masuda, S., Kosugi, T., Hara, H., Tsuneta, S., & Ogawara, Y. 1994, Natur, 371, 495
Melnikov, V. F. 2006 Solar Physics with the Nobeyama Radioheliograph, NSRO Rep. 1, ed. K. Shibasaki (Nobeyama, Nagano: NSRO), 11
Ni, L., Lin, J., Mei, Z., & Li, Y. 2015, ApJ, 812, 92
Oka, M., Birn, J., Battaglia, M., et al. 2018, SSRv, 214, 82
Oka, M., Phan, T. D., Krucker, S., Fujimoto, M., & Shinohara, I. 2010, ApJ, 714, 915
Onofri, M., Isliker, H., & Vlahos, L. 2006, PhRvL, 96, 151102
Petrosian, V., Donaghy, T. Q., & McTiernan, J. M. 2002, ApJ, 569, 459
Raymond, J. C., Krucker, S., Lin, R. P., & Petrosian, V. 2012, SSRv, 173 197
Ruan, W., Xia, C., & Keppens, R. 2020, ApJ, 896, 97
Seo, J., Guo, F., Li, X., & Li, H. 2024, ApJ, 977, 146
Share, G. H., Murphy, R. J., White, S. M., et al. 2018, ApJ, 869, 182
Siversky, T. V., & Zharkova, V. V. 2009, JPlPh, 75, 619
Sun, X., & Bai, X.-N. 2023, MNRAS, 523, 3328
Tsuneta, S., & Naito, T. 1998, ApJL, 495, L67
Turkmani, R., Cargill, P. J., Galsgaard, K., Vlahos, L., & Isliker, H. 2006, A&A, 449, 749
Vilmer, N., MacKinnon, A. L., & Hurford, G. J. 2011, SSRv, 159, 167
Warmuth, A., Mann, G., & Aurass, H. 2009, A&A, 494, 677
Xia, Q., Dahlin, J. T., Zharkova, V., & Antiochos, S. K. 2020, ApJ, 894, 89
Xia, Q., & Zharkova, V. 2020, A&A, 635, A116
Yan, L., Winter, H. D., Murphy, N. A., Jun, L., & Ning, W. 2013, PASJ, 65, 101
Yang, L.-P., Wang, L.-H., He, J.-S., et al. 2015, RAA, 15, 348
Ye, J., Cai, Q., Shen, C., et al. 2021, ApJ, 909, 45
Yu, S., Chen, B., Reeves, K. K., et al. 2020, ApJ, 900, 17
Zharkova, V. V., Arzner, K., Benz, A. O., et al. 2011, SSRv, 159, 357
Zharkova, V. V., & Gordovskyy, M. 2004, ApJ, 604, 884
Zhou, X., Büchner, J., Bárta, M., Gan, W., & Liu, S. 2016, ApJ, 827, 94
Zhu, B., Yan, H., Zhong, Y., et al. 2020a, AppMM, 78, 968
Zhu, B., Yan, H., Zhong, Y., et al. 2020b, AppMM, 78, 932
Ziegler, U. 2011, JCoPh, 230, 1035
Zimovets, I. V., Kuznetsov, S. A., & Struminsky, A. B. 2013, AstL, 39, 267